Atomic-Site-Specific Surface Valence-Band Structure from X-Ray Standing-Wave Excited Photoemission

Yanna Chen,[1] Leighton O. Jones,[2] Tien Lin Lee,[3] Anusheela Das,[1] Martín A. Mosquera,[4]
Denis T. Keane,[1] George C. Schatz,[2] and Michael J. Bedzyk[1,5,*]

[1]Department of Materials Science and Engineering, Northwestern University, Illinois 60208, USA
[2]Department of Chemistry, Northwestern University, Evanston, Illinois 60208, USA
[3]Diamond Light Source, Harwell Science and Innovation Campus, Didcot OX11 0DE, United Kingdom
[4]Department of Chemistry and Biochemistry, Montana State University, Bozeman, Montana 59717, USA
[5]Department of Physics and Astronomy, Northwestern University, Illinois 60208, USA

X-ray standing-wave (XSW) excited photoelectron emission was used to measure the site-specific valence band (VB) for ½ monolayer (ML) Pt grown on a SrTiO$_3$ (001) surface. The XSW induced modulations in the core level (CL), and VB photoemission from the surface and substrate atoms were monitored for three hkl substrate Bragg reflections. The XSW CL analysis shows the Pt to have a face-centered-cubic-like cube-on-cube epitaxy with the substrate. The XSW VB information compares well to a density functional theory calculated projected density of states from the surface and substrate atoms. Overall, this Letter represents a novel method for determining the contribution to the density of states by valence electrons from specific atomic surface sites.

Noble metal-oxide interfaces have important applications in both chemical and physical processes. Dramatic catalytic enhancement is found for low-coverage noble metals supported on oxide surfaces.[1–4] Pt on SrTiO$_3$ is one such case with importance to water-splitting photocatalysis [1,3]. The Pt/SrTiO$_3$ interface is also under consideration in thin film electronics for use in resistive random access memory devices [5]. As Pt layers are reduced down to several atomic layers in nanocrystals a larger fraction of the Pt atoms are at the interface which strongly influences catalytic properties [6]. For the Pt-support interface Pt atoms can interact with the TiO$_2$ support surface and withdraw electrons [7,8]. During a gas catalysis process, the pathway of the catalyzed reaction is governed by the atomic and electronic structures of the catalyst and the interface of catalyst-support [9]. While much research focuses on the Pt catalyst application, there are still open questions over the atomic and electronic properties, especially at the catalyst-support interface.

As a support for Pt, SrTiO$_3$ (STO) has a special morphological preference, since its cubic-P unit cell lattice constant ($a_{STO} = 3.905$ Å) is a close match to that of the face-centered-cubic (fcc) Pt lattice ($a_{Pt} = 3.924$ Å), and thus beneficial for obtaining an epitaxial interface. In previous work, fcc Pt nanocrystals on a STO (001) support were grown by molecular beam epitaxy, and x-ray standing-wave (XSW) excited Pt L_α x-ray fluorescence was used to find the different interfacial structures dependent on the Pt submonolayer coverage [10]. Using density functional theory, Stoltz et al. found different binding energies for the

Pt atoms that adsorb above the surface Ti and O atoms of the STO support [11]. However, the electronic structure in such classical heterostructures has not previously been described, but would provide a clearer structure-function relationship.

For the surface of a crystal, XSW analysis is advantageous for determining atomic positions of a particular surface atomic species relative to the substrate lattice [12–14]. The collection of XSW excited fluorescence [10,12,15] or photoelectrons [16–18] from electronic core levels has previously been used for determining specific atomic adsorption sites.

The valence electronic structure dictates the chemical and physical characteristics of a supported catalyst that lead to the formation and breaking of chemical bonds during a reaction [19]. While density functional theory (DFT) can be used to calculate the projected density of states from particular atoms at particular sites within the substrate or at the interface [20,21], conventional valence band (VB) photoemission does not directly provide such structural discrimination. Previously, XSW excited VB spectroscopy has been used to study site-specific valence-band properties for atoms within a bulk crystal [22–26]. Herein, we apply this XSW VB method to the novel study of atoms on a surface. To increase sensitivity we chose a high-Z element, namely submonolayer Pt on STO (001). We find that XSW excited VB spectroscopy has site-specific information from these surface atoms that compares well with DFT predictions.

The Pt submonolayer was grown on a 1×1 TiO$_2$ terminated STO (001) surface by pulsed laser deposition (PLD). X-ray fluorescence with comparison to a calibrated

standard was used to determine that the Pt coverage was ½ monolayer (ML) of a Pt (001) fcc layer (i.e., coverage = 6.5 Pt/nm²). At the Diamond Light Source I09 station back reflection XSW XPS [13] was performed for three different Bragg reflections: 002, 101, 111 of the STO (001) crystal. These three hkl's were chosen to enable triangulation of the Pt atomic positions relative to the STO lattice and to distinguish the VB contributions from each of the four elements. Pt $4f$, Ti $2p$, Sr $3d$, and O $1s$ core level (CL) spectra and VB spectra were collected while scanning the incident photon energy (E_γ) through each hkl Bragg reflection. The XSW induced modulations in the CL and VB photoelectron yields are shown in Fig. 1. (See Supplemental Material [27] for details).

For each $\mathbf{H} = hkl$ Bragg reflection, Fig. 1 shows the CL data fitted yield curves based on dynamical diffraction theory [13,14,40,41]:

$$Y(E_\gamma) = 1 + S_R R(E_\gamma)$$
$$+ 2|S_I|\sqrt{R(E_\gamma)}f_\mathbf{H} cos[\nu(E_\gamma) - 2\pi P_\mathbf{H} + \psi]. \quad (1)$$
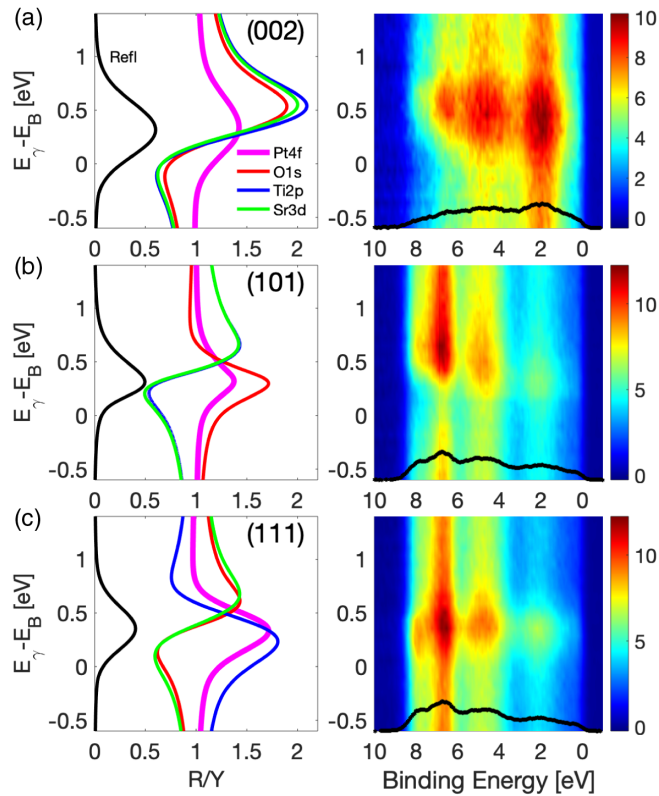
FIG. 1. Left: XSW excited Pt $4f$, O $1s$, Ti $2p$ and Sr $3d$ core-level yields and (right) valence band spectra collected while scanning the incident photon energy (E_γ) through the (a) 002, (b) 101, and (c) 111 SrTiO₃ Bragg reflections. (E_B is the photon energy predicted by Bragg's law.) The black line at the bottom of each 2D VB spectrum is a plot of the VB spectrum collected at an off-Bragg energy. The 002 off-Bragg VB spectrum is different because it was collected at a shallower (more surface sensitive) emission angle.

$R(E_\gamma)$ and $\nu(E_\gamma)$ respectively denote the reflectivity and XSW phase. Parameters $f_\mathbf{H}$ and $P_\mathbf{H}$ are the normalized amplitude and phase of the $\mathbf{H}$th Fourier component of the distribution of atoms being monitored by the spectrometer with elemental or even chemical-state specificity. S_R, $|S_I|$, and ψ, which are corrections for small nondipolar effects in the photoelectric cross section, are tabulated in Supplemental Material [27]. For our analysis we selected the origin of the STO cubic unit cell to be at the Sr site, which consequently is then the origin for each $P_\mathbf{H}$ scale. The Eq. (1) fit-determined $f_\mathbf{H}$ and $P_\mathbf{H}$ values for Pt $4f$ are listed in the Supplemental Material [27]. The fitted results for the substrate atoms follow the ideal perovskite structure of SrTiO₃.

The summation of these XSW XPS measured Fourier components and their symmetry equivalents generates a model-independent 3D map of the Pt atomic distribution [10,15,42,43]:

$$\rho(\mathbf{r}) = 1 + 2 \sum_{\mathbf{H} \neq -\mathbf{H}, \mathbf{H} \neq 0} f_\mathbf{H} \cos[2\pi(P_\mathbf{H} - \mathbf{H} \cdot \mathbf{r})]. \quad (2)$$

The 3D map is a projection of the Pt atomic distribution from the x-ray footprint (∼0.1 mm²) into a single STO cubic unit cell, which leads to fourfold and mirror symmetry along the c axis of the STO (001) surface. The generated 3D map of the Pt atomic distribution referenced to the STO lattice is shown in Fig. 2(a), where it can be seen that the Pt atoms form a fcc-like lattice registered to the STO lattice with a vertical shift. Based on the same domain averaging symmetry conditions described above, there are three symmetry inequivalent Pt sites in this arrangement, labeled A, B, and C. Note $C1$ and $C2$ are symmetry equivalent. The mean z displacements of Pt at the A, B, or $C1(C2)$ site as a fraction of a_{STO} relative to the bulklike SrO plane are listed in Table II.

To determine the occupation fraction α of correlated Pt in the A, B, and combined C sites, a fcc-like Pt model with two atomic layers is assumed based on the previously described XSW model-independent analysis portrayed in Fig. 2(a). Here the correlated Pt atoms are laterally constrained to occupy one of the A, B, or C sites. The values z and α are determined from a global least-squares fit of a model to the measured complex Fourier components as follows [10,15]:

$$F_\mathbf{H} = f_\mathbf{H} e^{2\pi i P_\mathbf{H}}$$
$$= e^{-2(\frac{\pi\sigma}{d_\mathbf{H}})^2}[\alpha_A e^{2\pi i \mathbf{H} \cdot \mathbf{r}_A}$$
$$+ \alpha_B e^{2\pi i \mathbf{H} \cdot \mathbf{r}_B} + \alpha_C(e^{2\pi i \mathbf{H} \cdot \mathbf{r}_{C1}} + e^{2\pi i \mathbf{H} \cdot \mathbf{r}_{C2}})]. \quad (3)$$

Here, $\mathbf{r}_A = (0, 0, z_A)$, $\mathbf{r}_B = (½, ½, z_B)$, $\mathbf{r}_{C1} = (½, 0, z_C)$, and $\mathbf{r}_{C2} = (0, ½, z_C)$ are unit cell fractional positions of the A, B, and C sites, respectively. $C1$ and $C2$ are symmetry equivalent. $d_\mathbf{H}$ is the STO d spacing. The XSW measured
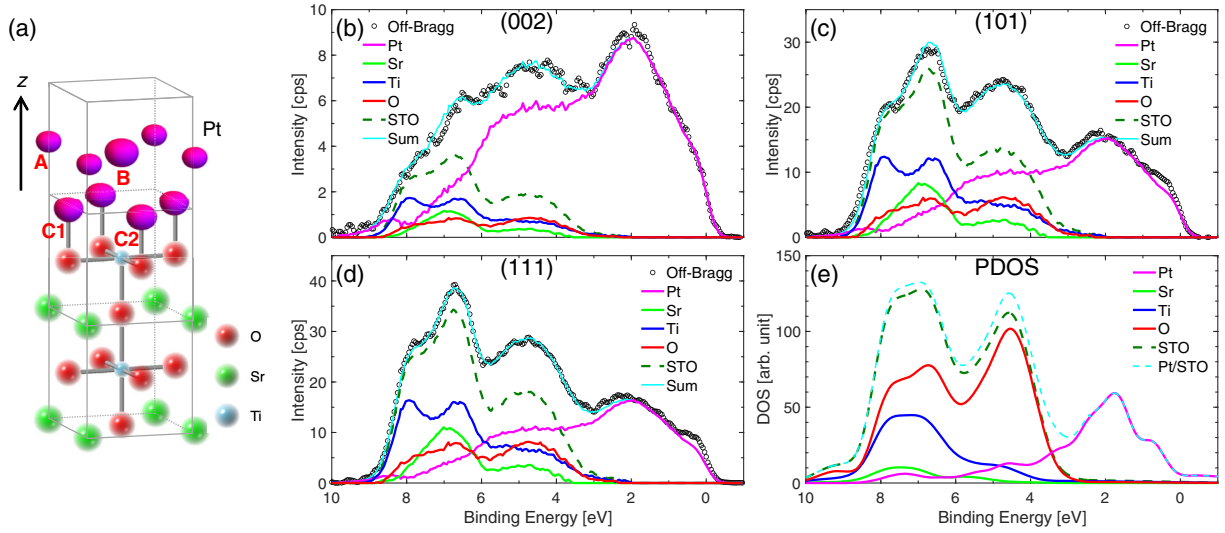
FIG. 2. (a) Based on Eq. (2) the model-independent XSW measured 3D Pt atomic distribution relative to STO unit cell shown with a TiO$_2$ terminated STO (001) surface. This contour plot is at $\rho = 0.8\rho_{max}$. A, B, and $C1(C2)$ refer to the three symmetry-inequivalent Pt sites. The origin is chosen to be at the bulk Sr site. The collected off-Bragg VB spectra and separated components from (b) 002, (c) 101, and (d) 111 SrTiO$_3$ Bragg reflections. (e) DFT calculated PDOS of the Pt/STO valence band. Note that the 002 VB spectrum is more sensitive to Pt because of the lower photoelectron emission angle.

f_H and P_H values are taken from Table I. The best-fit results, assuming a Pt atomic spread of $\sigma = 0.2$ Å in the Debye-Waller factor, are summarized in Table II. The ratio of occupation fraction $\alpha_A : \alpha_B : \alpha_C = 1 : 2 : 3$ is notably different from the ratio of ideal fcc Pt lattice which would be $1 : 1 : 2$; consistent with the C site being the bottom and therefore most populated layer. Summing all the occupation fractions at the three sites gives the fraction of correlated Pt atoms to be 0.61, meaning that 39% of the Pt are uncorrelated with the STO lattice.

The off-Bragg VB spectra shown at the bottom of Fig. 1 (right) are shown with better detail in Figs. 2(b)–2(d). These were collected on the low-photon-energy side of the Bragg peak at $E_\gamma - E_B = -1.1$ eV. To decompose these VB spectra into subspectra from the four atoms we use an approach similar to that used for an XSW VB study of bulk STO (001) [24], but now extended to include surface atoms. While this site-specific VB description is a direct outcome from DFT as illustrated for our case in Fig. 2(e), it cannot be determined from standard VB spectroscopy.

Referring to Fig. 1, we experimentally determine the site by observing which features in the VB fluctuate when the XSW antinode (or node) passes over a given bulk or surface atomic layer. This relies on Woicik's earlier finding that even though the valence electrons are spatially spread out from the atomic center, their photoelectric cross section is highly localized at the atomic center [44]. To get around the ambiguity of multiple atom types positionally overlapping in a given hkl direction, we chose a set of hkl reflections that have differing combinations of overlapping atom types. This sorting strategy is demonstrated in Fig. 1 (left), which shows the Eq. (1) fitted XSW modulations of Pt $4f$, Sr $3d$, Ti $2p$, and O $1s$ core level yields for the incident energy scans through the STO 002, 101, and 111 reflections. For the 002 all three bulk atom types overlap with each other, but not with the Pt atoms. This can be seen from the phases (or P_{002} values) of the four modulations in Fig. 1(a) and can be understood from the ball-and-stick diagrams of Fig. 2(a), which show respectively the bulk atomic positions at $P_{002} = 0$ coinciding with the (002) planes and the inward shift of the Pt atoms from these same planes at $P_{002} = -0.16$. For the 101 XSW scan of Fig. 1(b) we

TABLE I. Measured coherent fraction f_H and position P_H values for Pt atoms for the 3 hkl reflections. The model calculated values are determined from the global least-squares fit of the model described by Eq. (3) with values from Table II.

	XSW measured		Model calculated	
hkl	f_H	P_H	f_H	P_H
002	0.27	0.84	0.40	0.81
101	0.09	0.76	0.12	0.76
111	0.61	0.38	0.50	0.40

TABLE II. Results from the model-independent (MI) 3D atomic distribution in Fig. 2(a) and the Eq. (3) model-dependent (MD) analysis for Pt.

Site	*z* (MI)	*z* (MD)	α
A	0.41	0.43	0.10
B	0.38	0.33	0.20
$C1 + C2$	-0.11	-0.06	0.31

see that the Ti and Sr bulk atoms are in phase with each other at $P_{101} = 0$ and out of phase with the bulk O atoms at $P_{101} = \frac{1}{2}$. From Table I we see that $P_{101} = 0.76$ for the Pt atoms. We then use the 111 to put the Sr and O in phase with each other and out of phase with the Ti and Pt as seen in Fig. 1(c). The 2D plots on the right side of Fig. 1 are the VB spectra from -1 to 10 eV in binding energy collected at each incident photon energy step of the XSW scan with a range matching that of the left-side CL XSW scans.

Each binding energy (BE) point in the VB spectra (Fig. 1, right) is dependent on E_γ because the four atoms can have different $\Delta d/d$ diffraction plane positions. Due to the previously explained localized nature of the photo-electric effect, each atomic VB subspectrum has an XSW induced modulation that follows the CL yield for that atom as shown on the left side of Fig. 1. As detailed in the Supplemental Material [27] this relation is formalized with a matrix equation for each of the 251 binding energy (BE_i) points in each VB spectrum. The solutions to these over-determined sets of equations for each of three hkl reflections lead to the decomposition of the off-Bragg VB spectrum into subspectra for each constituent element as shown in Figs. 2(b)–(d). For each element, the three VB subspectra from the three hkl reflections differ by a scale factor that is due to differences in the experimental conditions, namely incident photon energy, incident inten-sity, sample-detector geometry [45], and photoelectric cross sections. We were able to create an all-inclusive set of simultaneous equations by normalizing for these differences, which led to a solution with higher fidelity.

To compare with the XSW XPS results, DFT calcula-tions were carried out for the projected densities of states (PDOS) of each element using the Spanish initiative for electronic simulations with thousands of atoms (SIESTA) code. The 3D model generated from the XSW CL photo-emission analysis was used to construct an atomistic super cell. The PDOS were computed using the conju-gate-gradient algorithm, with the generalized gradient approximation Perdew–Burke–Ernzerhof functional and a broadening of 0.4 eV. The PDOS of each element as a summation of its valence electronic states is shown in Fig. 2(e).

In Fig. 3 we compare the DFT calculations to the experimental results by converting each orbital PDOS to photoelectron yield (see the Supplemental Material [27]). Here the photoelectric effect cross section ratios are corrected because the solid-state VB is significantly under-estimated by the tabulated atomic cross section [23,24]. The Pt subspectrum in Fig. 3(a) has mainly Pt $5d$ states and $4f$ states located near the Fermi level. Note that the DFT calculated Pt subspectrum corresponds to correlated Pt as depicted in Fig. 2(a), whereas the measured Pt VB sub-spectrum has a 39% contribution from uncorrelated Pt atoms. Given this factor, the difference between calculated and experimental yields is reasonable. The calculated Sr
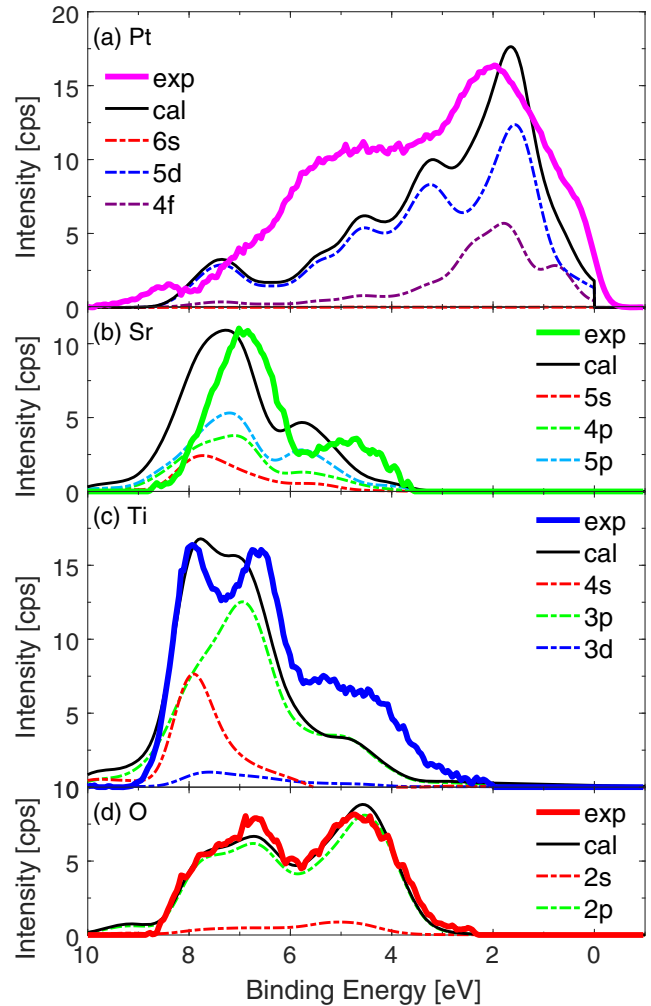
FIG. 3. Decomposed (a) Pt, (b) Sr, (c) Ti, and (d) O valence band spectra in 111 off-Bragg condition based on experimental data (exp) compared with DFT calculated PDOS (s, p, d, or f states) converted to photoelectron yield (cal). Note that the sum of all four experimental subspectra is equivalent to the spectrum labeled Sum in Fig. 2(d).

yield in Fig. 3(b) reproduces the experimental yield through $5s$, polarized $5p$, and semicore $4p$ states. We note a peak shift close to 1 eV [Fig. 3(b)], likely due to an inherent shift already present in the original SIESTA pseudopotential (free of semicore states). The calculated Ti yield in Fig. 3(c) includes $3d$ and $4s$ states, and the Ti $3p$ semicore was introduced to create the features at 4–7 eV. The calculated O yield [Fig. 3(d)] perfectly reproduces the experimental yield with a majority of O $2p$ state. The features of Sr, Ti, and O follow the previous XSW VB results for bulk STO [24].

Compared with the valence-band spectrum of bulk metallic Pt [46], our measurement in Fig. 3(a) is missing a strong peak right at the Fermi edge, which could correspond to a reduction of electronic states due to the orbital hybridization of Pt $4f$ with O atoms. DFT was used

to study this effect by comparing to a model with Pt atoms at C sites only [Fig. 2(a)] located atop of O atoms without the top Pt layer (A and B sites). Here the Pt $4f$ states at the Fermi level are reduced to zero (see the Supplemental Material [27]). A round shoulder, rather than a peak, at the Fermi edge for the Pt subspectrum further confirms the Pt—Pt bond in the Pt monolayer and the Pt—O bond at the Pt/SrTiO$_3$ interface.

In summary, the 3D atomic distribution of ½ ML Pt on the SrTiO$_3$ (001) surface was measured from the XSW excited core level Pt $4f$ yields for three hkl Bragg reflections. This provided a model for a density functional theory calculation that was used to interpret the XSW site-specific valence-band measurements. The XSW XPS core level yields of Pt $4f$, Sr $3d$, Ti $2p$, and O $1s$ make it possible to separate out the Pt, Sr, Ti, and O contributions to the valence-band spectrum. It is presently possible to make such measurements for monolayer coverages of high-Z surface atoms like Pt with third generation synchrotron x-ray sources. The predicted 500-fold gain in brightness from the next generation of x-ray sources should make it possible to apply this method to lower-Z surface atoms, including 2D van der Waals heterostructures with interesting quantum properties [47].

*Corresponding author.
bedzyk@northwestern.edu

[1] R. G. Carr and G. A. Somorjai, Nature (London) **290**, 576 (1981).

[2] M. S. Chen and D. W. Goodman, Science **306**, 252 (2004).

[3] S. Ikeda, K. Hirao, S. Ishino, M. Matsumura, and B. Ohtani, Catal. Today **117**, 343 (2006).

[4] O. Rosseler, M. V. Shankar, M. Karkmaz-Le Du, L. Schmidlin, N. Keller, and V. Keller, J. Catal. **269**, 179 (2010).

[5] T. Menke, R. Dittmann, P. Meuffels, K. Szot, and R. Waser, J. Appl. Phys. **106**, 114507 (2009).

[6] M. Cargnello, V. V. Doan-Nguyen, T. R. Gordon, R. E. Diaz, E. A. Stach, R. J. Gorte, P. Fornasiero, and C. B. Murray, Science **341**, 771 (2013).

[7] A. Lewera, L. Timperman, A. Roguska, and N. Alonso-Vante, J. Phys. Chem. C **115**, 20153 (2011).

[8] G. Kennedy, L. R. Baker, and G. A. Somorjai, Angew. Chem. **126**, 3473 (2014).

[9] C. Xie, Z. Niu, D. Kim, M. Li, and P. Yang, Chem. Rev. **120**, 1184 (2020).

[10] Z. Feng, A. Kazimirov, and M. J. Bedzyk, ACS Nano **5**, 9755 (2011).

[11] S. Stoltz, D. Ellis, and M. Bedzyk, Surf. Sci. **633**, 8 (2015).

[12] J. A. Golovchenko, J. R. Patel, D. R. Kaplan, P. L. Cowan, and M. J. Bedzyk, Phys. Rev. Lett. **49**, 560 (1982).

[13] J. Zegenhagen and A. Kazimirov, *X-ray Standing Wave Technique, Principles and Applications* (World Scientific, Singapore, 2013).

[14] D. P. Woodruff, Rep. Prog. Phys. **68**, 743 (2005).

[15] Z. Feng, C.-Y. Kim, J. W. Elam, Q. Ma, Z. Zhang, and M. J. Bedzyk, J. Am. Chem. Soc. **131**, 18200 (2009).

[16] I. Kröger, B. Stadtmüller, C. Kleimann, P. Rajput, and C. Kumpf, Phys. Rev. B **83**, 195414 (2011).

[17] J. D. Emery, B. Detlefs, H. J. Karmel, L. O. Nyakiti, D. K. Gaskill, M. C. Hersam, J. Zegenhagen, and M. J. Bedzyk, Phys. Rev. Lett. **111**, 215501 (2013).

[18] G. Heimel, S. Duhm, I. Salzmann, A. Gerlach, A. Strozecka, J. Niederhausen, C. Bürker, T. Hosokai, I. Fernandez-Torrente, G. Schulze *et al.*, Nat. Chem. **5**, 187 (2013).

[19] B. Hammer, Top. Catal. **37**, 3 (2006).

[20] S. A. Chambers, T. Droubay, T. C. Kaspar, M. Gutowski, and M. Van Schilfgaarde, Surf. Sci. **554**, 81 (2004).

[21] H. Seo and A. A. Demkov, Phys. Rev. B **92**, 245301 (2015).

[22] J. C. Woicik, E. J. Nelson, D. Heskett, J. Warner, L. E. Berman, B. A. Karlin, I. A. Vartanyants, M. Z. Hasan, T. Kendelewicz, Z. X. Shen, and P. Pianetta, Phys. Rev. B **64**, 125115 (2001).

[23] J. C. Woicik, E. J. Nelson, L. Kronik, M. Jain, J. R. Chelikowsky, D. Heskett, L. E. Berman, and G. S. Herman, Phys. Rev. Lett. **89**, 077401 (2002).

[24] S. Thiess, T.-L. Lee, F. Bottin, and J. Zegenhagen, Solid State Commun. **150**, 553 (2010).

[25] S. Nemšák, M. Gehlmann, C.-T. Kuo, S.-C. Lin, C. Schlueter, E. Mlynczak, T.-L. Lee, L. Plucinski, H. Ebert, I. Di Marco *et al.*, Nat. Commun. **9**, 3306 (2018).

[26] C.-T. Kuo, S.-C. Lin, J.-P. Rueff, Z. Chen, I. Aguilera, G. Bihlmayer, L. Plucinski, I. L. Graff, G. Conti, I. A. Vartanyants *et al.*, Phys. Rev. B **104**, 245105 (2021).

[27] See Supplemental Material at http://link.aps.org/supplemental/10.1103/PhysRevLett.128.206801 for details on surface preparation, characterization, data analysis and DFT, which includes Refs. [28–39].

[28] M. Kawasaki, K. Takahashi, T. Maeda, R. Tsuchiya, M. Shinohara, O. Ishiyama, T. Yonezawa, M. Yoshimoto, and H. Koinuma, Science **266**, 1540 (1994).

[29] R. Herger, P. Willmott, O. Bunk, C. Schleptz, B. Patterson, and B. Delley, Phys. Rev. Lett. **98**, 076102 (2007).

[30] Diamond Light Source I09 Beamline Layout, https://www.diamond.ac.uk/Instruments/Structures-and-Surfaces/I09/Beamline-layout.html.

[31] B. W. Batterman and H. Cole, Rev. Mod. Phys. **36**, 681 (1964).

[32] N. A. Fairley, CasaXPS, Casa Software Ltd, 2020.

[33] R. T. Haasch, E. Breckenfeld, and L. W. Martin, Surf. Sci. Spectra **21**, 87 (2014).

[34] E. J. Nelson, J. C. Woicik, P Pianetta, I. A. Vartanyants, and J. W. Cooper, Phys. Rev. B **65**, 165219 (2002).

[35] M. B. Trzhaskovskaya, V. I. Nefedov, and V. G. Yarzhemsky, At. Data Nucl. Data Tables **77**, 97 (2001).

[36] M. B. Trzhaskovskaya, V. I. Nefedov, and V. G. Yarzhemsky, At. Data Nucl. Data Tables **82**, 257 (2002).

[37] A. Jablonski, F. Salvat, and C. J. Powell, *NIST Electron Elastic Scattering Cross-Section Database, Version 3.2, SRD 64* (National Institute of Standarts and Technology, Gaithersburg, MD, 2010).

[38] W. S. M. Werner, W. Smekal, and C. J. Powell, *Simulation of Electron Spectra for Surface Analysis (SESSA) 2.2.0* (National Institute of Standards and Technology, Gaithersburg, MD, 2021).

[39] J. E. Carnes and A. M. Goodman, J. Appl. Phys. **38**, 3091 (1967).

[40] G. van Straaten, M. Franke, F. C. Bocquet, F. S. Tautz, and C. Kumpf, J. Electron Spectrosc. Relat. Phenom. **222**, 106 (2018).

[41] D. P. Woodruff, Nucl. Instrum. Methods Phys. Res., Sect. A **547**, 187 (2005).

[42] L. Cheng, P. Fenter, M. J. Bedzyk, and N. C. Sturchio, Phys. Rev. Lett. **90**, 255503 (2003).

[43] J. S. Okasinski, C. Y. Kim, D. A. Walko, and M. J. Bedzyk, Phys. Rev. B **69**, 041401(R) (2004).

[44] J. C. Woicik, E. J. Nelson, and P. Pianetta, Phys. Rev. Lett. **84**, 773 (2000).

[45] A. X. Gray, J. Minr, L. Plucinski, M. Huijben, A. Bostwick, E. Rotenberg, S. H. Yang, J. Braun, A. Winkelmann, G. Conti *et al.*, Europhys. Lett. **104**, 17004 (2013).

[46] M. Engelhard and D. Baer, Surf. Sci. Spectra **7**, 1 (2000).

[47] X. Liu and M. C. Hersam, Nat. Rev. Mater. **4**, 669 (2019).